Formulation of carbon black-ionomer dispersions for thin film formation in fuel cells

Eva Hoffmann, Su Zhang, Martin Thoma, Cornelia Damm, Wolfgang Peukert*

Institute of Particle Technology (LFG), Friedrich-Alexander-Universität Erlangen-Nürnberg (FAU), Cauerstraße 4, D-91058 Erlangen, Germany

ARTICLE INFO

ABSTRACT

The performance of proton exchange membrane fuel cells (PEMFC) is strongly determined by the structure and composition of the electrode layer. The interactions between the ionomer, carbon black particles, and solvent affect the suspension properties and thus the layer morphology. We analyze the effect of the ionomer-to-carbon (I/C) weight ratio for two different types of carbon black on the suspension and layer characteristics. Highly branched carbon blacks with a high surface area tend to form less cracked layers. As less branched carbons can pack together more closely, a smaller pore size results in a larger capillary pressure during drying and thus more cracks. The added ionomer adsorbs on the carbon particles and improves the colloidal stability of the carbon black particles. The carbon black aggregates are thus smaller, resulting in closer packing and thinner layers. Moreover, the addition of the ionomer increases the critical coating thickness (CCT) of the layers because drying stresses are dissipated by the deformation of the ionomer, preventing crack formation. An optimum I/C weight ratio is identified for optimal layer formation and minimized crack formation.

© 2018 Chinese Society of Particuology and Institute of Process Engineering, Chinese Academy of Sciences. Published by Elsevier B.V. All rights reserved.

Introduction

Proton exchange membrane fuel cells (PEMFCs) are promising candidates for a clean and efficient power supply for vehicles owing to their high energy efficiency and low emissions. The core of a PEMFC is the membrane electrode assembly (MEA), which consists of two electrodes and a solid ionomer membrane as the electrolyte. The structure of the electrodes depends on the material properties and process conditions, and therewith significantly affects the efficiency of a PEMFC. The electrode layers consist of catalyst particles (commonly Pt) on carbon black carrier particles imbedded in a perfluorinated sulfonic acid (PFSA) ionomer network (Holdcroft, 2014; Uchida, 1995, 1996, 1998). The carbon black particles provide the electrical conductivity of the layer, whereas the ionomer governs the proton transport within the electrode. PFSA ionomers consist of a hydrophobic tetrafluoroethylene backbone and hydrophilic perfluorinated vinyl ether side chains with a sulfonic acid end group (Mauritz & Moore, 2004). Incorporating the ionomer into the catalyst layer (CL) increases the contact area between the ionomer, catalyst, and reaction gas and thus the fuel cell performance (Giorgi, Antolini, Pozio, & Passalacqua, 1998; Watanabe, Tomikawa, & Motoo, 1985). Ionomers are characterized by their equivalent weight (EW), which is defined as the mass of dry ionomer per mole of sulfonic acid group (Mauritz & Moore, 2004). The long-side-chain PFSA ionomer Nafion® with an equivalent weight of approximately 1000–1100 g/mol_{SO3} is still the most commonly used and studied ionomer. Short-side-chain (SSC) ionomers with lower EW have recently become more popular owing to their enhanced proton conductivity, higher glass transition temperature, and better thermal stability (Jeon et al., 2010; Kreuer et al., 2008; Marrony et al., 2013). Moreover, SSC ionomers have been shown to improve fuel cell performance, as electrode layers are more porous and better coverage of the catalyst particles is achieved (Park, Kakinuma, Uchida, Watanabe, & Uchida, 2015; Peron et al., 2011; Zhao et al., 2013). For optimum fuel cell performance, the use of an appropriate amount of ionomer is indispensable, as the ionomer content affects the ionic conductivity, catalytic activity, electronic transport, and gas permeability through the layer. At too low ionomer contents, the catalyst particles are insufficiently covered with ionomer, and therefore, catalyst utilization and ionic conductivity are poor, whereas the network provides good electronic conduction. At an optimum ionomer concentration, sufficient percolating networks for both ion and electron transport are formed. However, when the ionomer content is increased

* Corresponding author.
   E-mail addresses: eva.hoffmann@fau.de (E. Hoffmann), su.zhang@fau.de
(S. Zhang), martin.t.thoma@fau.de (M. Thoma), cornelia.damm@fau.de (C. Damm),
wolfgang.peukert@fau.de (W. Peukert).

Symbols

A	Projection area, μm^2
b	Width of substrate, mm
c_{eq}	Equilibrium concentration of ionomer in water, g/L
C	Circumference of particle, μm
CCT	Critical coating thickness, μm
d_{002}	Mean interlayer distance between carbon layers, nm
$d(t)$	Cantilever bending, mm
E	Young's modulus/elastic modulus, Pa
E_s	Young's modulus/elastic modulus of substrate, Pa
f	Fitting parameter (growth function)
f_t/f_0	Frictional factor
g	Gravitational acceleration (9.81 m/s^2), m/s^2
G	Shear modulus of particles, Pa
G'	Storage modulus, Pa
G''	Loss modulus, Pa
G-position	Position of G-peak (Raman), cm^{-1}
h_{layer}	Layer/film thickness, μm
$h_c(t)$	Coating thickness, μm
h_{gap}	Gap height of doctor blade, μm
h_s	Cantilever thickness, μm
h_{wet}	Wet film thickness, μm
I_D	D-Peak intensity
I_G	G-Peak intensity
L	Effective length of substrate, mm
l_{flaw}	Length of a flaw/initiation crack, m
K_{eq}	Association constant, L/g
M	Coordination number
$m_{carbon\ black}$	Carbon black mass, g
$m_{ionomer}$	Ionomer mass, g
$\Delta m(t)$	Coating mass loss, g
n	Power law index for Ostwald-de-Waele model
p_{cap}	Capillary pressure, Pa
$p_{cap,max}$	Maximum capillary pressure, Pa
Q_3	Cumulative volume distribution, %
r_{rot}	Rotation radius, mm
r	Particle radius, μm
r_p	Pore radius, μm
R_{RMS}	Roughness (root mean square), nm
RST	Relative sedimentation time, s^2/m^2
s	Sedimentation coefficient, sved
$S_{A,C}$	Specific surface area of carbon, m^2/g
$S_{A,C,access}$	Accessible specific surface area of carbon, m^2/g
$S_{MP,C}$	Surface area of micropores of carbon, m^2/g
T	Transmission, %
T_0	Start transmission, %
T_{end}	End transmission, %
t_{sed}	Sedimentation time, s
t_{50}	Sedimentation time at $T_{end}/2$, s
u	Sedimentation velocity, m/s
$V_{carbonblack}$	Carbon black volume, cm^3
$V_{ionomer}$	Ionomer volume, cm^3
V_p	Particle volume, cm^3
x	Particle diameter, μm
x_{area}	Area equivalent particle diameter, μm
X_{layer}	Mass loading of layer per area, g/cm^3
x_V	Volume equivalent particle diameter, μm
$x_{50,3}$	Median volumetrically particle size, μm

Greek letters

γ	Amplitude, %
γ_L	Surface tension of liquid, N/m
γ_S	Surface tension of a solid, N/m
$\dot{\gamma}$	Shear rate, s^{-1}
Γ_{eq}	Equilibrium coverage, g/g
Γ_{sat}	Saturation surface coverage, g/g
ε	Porosity
η	Dynamic viscosity, Pa s
η_s	Dynamic solvent viscosity, Pa s
θ	Bragg diffraction angle, °
θ_{SL}	Contact angle between solid and liquid, °
κ	Fitting parameter for Ostwald-de-Waele model, Pa s
λ	Wavelength, nm
ν	Poisson's ratio
ν_s	Poisson's ratio of substrate
ρ	Density, kg/m^3
$\rho_{carbon\ black}$	Carbon black density (average: 1.9 g/cm^3), kg/m^3
$\rho_{ionomer}$	Ionomer density (2.0 g/cm^3), kg/m^3
ρ_{layer}	Layer density, kg/m^3
$\rho_{mixture}$	Mixture density, kg/m^3
ρ_p	Particle density, kg/m^3
ρ_s	Solvent density, kg/m^3
σ_c	Cracking stress, Pa
σ_{crit}	Critical cracking stress, Pa
$\sigma(t)$	Drying stress, Pa
τ	Shear stress, Pa
τ_0	Yield stress, Pa
ϕ_{rcp}	Particle volume fraction at random close packing
ω	Angular frequency/angular velocity, rad/s

beyond the optimum concentration, although the ionic conductivity is still good, the electronic pathways and gas diffusion are hampered (Gode, Jaouen, Lindbergh, Lundblad, & Sundholm, 2003; Passalacqua, Lufrano, Squadrito, Patti, & Giorgi, 2001). Moreover, it has been shown that increasing the polymer content in the carbon black layer reduces the porosity (Giorgi et al., 1998; Park, Tokiwa, Kakinuma, Watanabe, & Uchida, 2016; Uchida, 1996; Watanabe et al., 1985; Yu, Roller, Mustain, & Maric, 2015). Two different characteristic pore sizes exist in the final electrode layers, namely primary pores with diameters smaller than 10–100 nm and larger secondary pores (Komoda et al., 2009; Uchida, 1996; Watanabe et al., 1985; Yu et al., 2015). As the primary pores are not affected by the polymer, the secondary pores are blocked with successive addition of ionomer. The primary pores are the voids inside the carbon black aggregates consisting of primary particles, whereas the secondary pores are the spaces within the agglomerates. Soboleva et al. (2010) even distinguishes between micropores inside the carbon primary particles (<2 nm), mesopores inside the aggregates (2–20 nm), and macropores, which are voids between the agglomerates (>50 nm). The pore-volume reduction with increasing ionomer content is accompanied by a decrease of the active surface area of the Pt/C particles (Yu et al., 2015). The optimum ionomer-to-carbon (I/C) ratio depends on the material properties of the ionomer and carbon black as well as on the platinum loading of the carbon black particles and thus needs to be determined for every material match.

For electrode layer preparation, a catalyst ink consisting of catalyst particles and PFSA ionomer dispersed in a solvent is coated on a decal substrate by doctor blading (Bender, Zawodzinski, & Saab, 2003; Wilson & Gottesfeld, 1992). Several other coating and process methods, e.g. spraying techniques and direct coating on the ionomer membrane or the gas diffusion layer, are described in the literature (Holdcroft, 2014; Ngo, Yu, & Lin, 2013; Yu et al., 2015). The selection of a suitable solvent composition is essential to obtain good-quality electrode layers (Holdcroft, 2014). Several research groups have shown that the use of slow-drying (high boil-

ing point) solvents results in reduced drying stresses and less crack formation within a film (Huang et al., 2011; Jung, Kim, & Yi, 2012; Perera & van den Eynde, 1983; Yang et al., 2004). The structure and morphology of the catalyst layers govern the fuel cell performance. In addition to being determined by the material composition and properties, the electrode structure is mainly affected by the interactions between the catalyst particles, ionomer, and solvent in the ink and during drying. Therefore, the complex interplay between the ionomer, catalyst, and solvent has been extensively investigated by many research groups (Eguchi et al., 2012; Gode et al., 2003; Jeon et al., 2010; Jung et al., 2012; Lai, Lin, Ting, Chyou, & Hsueh, 2008; Lee & Hwang, 2008; Ngo et al., 2013; Sasikumar, Ihm, & Ryu, 2004; Shukla, Bhattacharjee, Weber, & Secanell, 2017).

It is well known that the ionomer acts as a stabilizer for the carbon black particles and improves the ink stability (Shukla et al., 2017). Based on experiments in different dispersion media, Shukla et al. derived a model to describe the ink stability and aggregation rates that accounts for the van der Waals attraction and Coulomb repulsion. Several studies on the adsorption behavior of ionomer onto carbon black or carbon black/platinum particles have shown that the amount of adsorbed ionomer depends on the accessible surface area and the surface functional groups of the carbon (Andersen et al., 2014; Ma, Chen, Jogensen, Stein, & Skou, 2007; Mizukawa & Kawaguchi, 2009). Because of the stabilization, the size of the carbon black agglomerates decreases (Shukla et al., 2017), resulting in lower suspension viscosity owing to the reduction of attractive particle interactions (Gallo Stampino et al., 2009; Mizukawa & Kawaguchi, 2009). However, when the amount of catalyst or carbon black particles is increased, higher viscosities are obtained because of the stronger attractive particle interactions resulting from the decreasing inter-particle distances (Gallo Stampino et al., 2009; Komoda et al., 2009). Komoda et al. (2009) further showed that the viscosity is a good indicator of the formation and break-up of particle clusters during mixing and that the dispersibility of the Pt/C particles strongly depends on the amount of Nafion in the slurry. Gallo Stampino et al. (2009) showed that the viscosity mainly determines the film thickness, independent of the composition of the suspension.

The main focus of ionomer/catalyst formulation investigations has been the electrochemical fuel cell performance, and the effect of the polymer-to-carbon ratio on the morphology of the catalyst layers has been poorly investigated. In particular, avoidance of cracking is crucial in electrode formation, as cracking can result in by-pass flow of the gases, interruption of the protonic and electrical pathways, and water accumulation within the layers. However, recent results obtained by Ahn et al. (2018) indicate that the generation of guided cracks in the cathode layers improve MEA performance because of the improved water transport. To obtain a better understanding of the effect of the ionomer/catalyst interplay on film formation, and especially the layer cracking behavior, we investigated the effect of the carbon black type and I/C weight ratio on the suspension properties, drying behavior, and layer characteristics of pseudo-catalyst layers using only the ionomer and two carbon black types without catalyst particles. In particular, the mechanisms during drying and cracking are not yet fully understood. Even though a large number of publications have described and investigated the mechanisms during drying of colloidal films, most experiments and simulations were conducted using monodisperse, spherical model particles (Russel, 2011; Singh, Bhosale, & Tirumkudulu, 2009; Singh & Tirumkudulu, 2007; Tirumkudulu & Russel, 2005). In the current work, we form layers consisting of two species (the ionomer and fractal carbon black) and investigate the effect of the suspension properties on the later layer characteristics, especially in terms of cracking. As not only cracking but also the final morphology of the catalyst layer depend on the heterogeneous structure of the educts and their interactions with each other

(Holdcroft, 2014), the objective of this work was to investigate the effect of the type of carbon black and the ionomer concentration on the suspension properties, film formation, and drying of layers for PEM fuel cell electrodes.

Materials and methods

Materials

The SSC ionomer Aquivion® D79-25BS (Solvay) with an EW of 790 g/mol$_{SO3}$ was used. This ionomer is commercially available as an aqueous dispersion with a polymer content of 25 wt%. In water, a single ionomer molecule exhibits particle sizes of 7–8 nm, as measured by analytical ultracentrifugation in our lab (Wawra et al., 2018). Two carbon blacks (CB1 and CB2) were provided by Greenerity GmbH and characterized in our lab, see Chapter "Characterization of carbon blacks". The CB1 used was Vulcan XC 72. CB2 is an unknown amorphous high surface carbon black. For the solvent, a mixture consisting of 13 wt% distilled water and 87 wt% of diacetone alcohol (DAA, also known as 4-hydroxy-4-methyl-2-pentanone, 99%, purchased from Sigma Aldrich) was used.

Experimental methods

Carbon black powder characterization

The mass specific surface area of the carbon blacks was determined from nitrogen gas sorption using a Nova 4200e device (Quantachrome, Odelzhausen, Germany). The samples were degassed under vacuum ($p < 1.3 \times 10^{-5}$ bar) at 120 °C for 2 h prior to measurement. The Brunauer–Emmett–Teller (BET) model (Brunauer, Emmett, & Teller, 1938) was used for data evaluation to determine the specific surface area $S_{A,C}$ and surface area of the micropores $S_{MP,C}$.

Raman spectra were recorded using a confocal Raman spectrometer (LabRAM HR Evolution, Horiba, Japan) in the wave number range from 1000 to 1800 cm^{-1}. The carbon blacks were dispersed in ethanol via ultrasound and dropped on a silicon wafer. For the measurement, a 50 × objective and the second harmonic of a Nd-YAG laser (532 nm) were used. An 1800 grid size was selected. The laser beam was attenuated to 5% of its original intensity to avoid damage of the sample. The integration time per data point was set to 30 s using two accumulations. An automated movable table (Märzhäuser, Germany) allowed us to record two-dimensional maps (5 × 6 data points = 30 single Raman spectra). The Raman spectra were evaluated according to the approach proposed by Ferrari and Robertson (2004) by fitting the spectra with two single Lorentz functions for the D and G peaks. From the maximum intensities of the fitted peaks, the I_D/I_G ratio was calculated. The G-position refers to the wave number at which the maximum of the G-peak fit was observed.

X-ray diffraction (XRD) analysis of the carbon blacks was performed using an AXS D8 Advance diffractometer (Bruker, USA). Diffractograms were recorded at ambient temperature in the range of $2\theta = 10°$–$90°$ with a Cu Kα radiation source (wavelength $\lambda = 154.06$ pm). The integration time for each step was 1.5 s, and a step width of 0.04° was used. The voltage and current were set to 30 kV and 40 mA, respectively. The (002) peak was fitted by a Gaussian function, and the interlayer distance d_{002} (in nm) between the carbon layers was determined from the Bragg diffraction angle θ (in °) at the maximum of the (002) peak using the Bragg equation (Eq. (1)):

$$d_{002} = \frac{\lambda}{2 \sin \theta}.$$

(1)

The particle densities were determined using a helium pycnometer (AccuPyc 1330 V2.02N; Micromeritics, USA) at ambient

temperature. The sample (mass: 1–2.5 g) was filled in an 11.49 cm^3 aluminum cylinder and pressurized with helium gas. From the volume difference between the empty and full cylinder, the carbon black density was calculated. The reported values are the means of five measurements.

Dispersion

The suspensions were prepared with 4 wt% carbon black (CB), whereas the amount of ionomer was varied to achieve I/C weight ratios of 0, 0.2, 0.5, and 1.0 (Table 1), which results in varied overall solid contents of the suspension. Additional suspensions with I/C ratios of 0.1, 0.35, and 0.75 were prepared with CB1 (marked with * in Table 1). A mixture consisting of 13 wt% distilled water and 87 wt% DAA was used as the solvent.

After pre-mixing the materials in a beaker on a magnetic stirring plate, the particles were dispersed using a rotor-stator mixer (Ultraturrax T25, IKA) with an S 25 N – 25 F dispersion tool. For the dispersion, 200 g of the pre-suspension was added to a 250-mL screw cap flask, and a rotational speed of 11,000 rpm was applied for 30 min. The process temperature was adjusted using a water bath and a recirculating cooler (FL300, Julabo GmbH, Germany), which was set to 25 °C. During grinding, the flask opening was sealed with Parafilm to prevent evaporation. After grinding, the suspension was permanently stirred with a magnetic stirrer (Topolino, IKA-Werke GmbH & Co. KG, Germany) at ~750 rpm. Analysis of the suspension properties and formation of the layers was conducted 2 days after preparation of the suspension. This time interval was kept constant for all the samples.

Particle size analysis

Particle size distributions (PSD) of the product suspensions were obtained by laser diffraction using a Mastersizer 2000 with a Hydro 2000S wet dispersion unit (Malvern, UK). The suspensions were diluted with deionized water (1–3 droplets of suspension in ~15 mL water) prior to measurement. The measurements were performed with 5% ultrasonic treatment at an optical obscuration of approximately 10%–13%. Each sample was measured five times, and the mean value was calculated.

Rheological characterization

Rheological measurements were conducted with a MCR 302 rheometer (Anton Paar, Austria) at 25 °C. A plate–plate geometry (diameter: 25 mm) with a gap height of 1 mm was used. Flow curves were obtained by varying the shear rate between 0.01 and 1000 s^{-1} and backwards. Oscillating experiments with constant angular frequency (ω = 10 rad/s) and varying amplitude (γ = 0.01%–100%) (amplitude sweep) were also performed. Prior to each measurement, the suspension was pre-treated at 1 s^{-1} for 2 min, followed by a resting time of 3 min. New samples were used for each measurement.

Colloidal stability analysis

Sedimentation analysis by centrifugation was performed using a LUMiSizer, a multisample analytical centrifuge manufactured by L.U.M. GmbH, Berlin, Germany. Using this method, which is described in detail by Detloff, Sobisch, and Lerche (2007), the sedimentation stability of the suspensions was determined by measuring the transmission profiles as a function of radial position and time. Each suspension was double-tested by filling two PA cuvettes with an optical pathway of 2 mm. The temperature was set to 25 °C, and a light source with a wavelength of 865 nm was used. A rotor speed of 2064 rpm (1500 × g at a mean rotational radius of 105 mm) was applied for all the centrifugations. Every measurement consisted of 999 single spectra. The frequency of spectra detection decreased with centrifugation time. The first 350 spectra were recorded every 3 s, whereas at the end of the centrifugation run,

an interval time between each spectrum of 600 s was employed for the last 50 spectra. The total centrifugation time was 22.3 h.

Cantilever deflection method

To determine the cracking stresses and mass loss during drying, the cantilever deflection method was used (Fu, Eckstein, Dellert, & Roosen, 2015). The suspension was coated by hand onto a cantilever stainless-steel substrate (1.4310; length: 103 mm; width: 11.6 mm; thickness: 300 μm; HASBERG Schneider GmbH, Germany) by means of a POM coating mask with a defined gap height of 245 μm. The mass loss was determined using an analytical balance. At the free end of the cantilever, the curvature change due to drying stresses was determined by a laser sensor (Laser B), whereas the drying shrinkage of the layer was detected at the fixed end (Laser A). The drying stresses were calculated using the modified Corcoran equation (Eq. (17)) (Fu et al., 2015).

Film formation via doctor blading

The layers were created with the film applicator Coatmaster 510 and the Multicator 411 doctor blade (film width: 80 mm) of Erichsen GmbH & Co. KG, Germany. The suspensions were coated onto a Mylar A PET foil (foil thickness: ~100 μm) at a speed of 100 mm/s. With the help of a vacuum suction plate, the foil was locally fixed. The layers were formed at ambient temperature. The layers remained on the vacuum suction plate until they were visually dried. Afterwards, the layers were tempered at 80 °C for ~10 min to remove any residual solvent. The layer thicknesses h_{layer} of the dried layers were measured using a caliper. To determine the layer mass loading per area X_{layer}, a 4 × 4 cm^2 piece was cut out, and the mass of the layer was gravimetrically determined from the difference between the mass layer and the substrate and the substrate alone after peeling off the layer.

Scanning electron microscopy (SEM) and optical microscopy analysis

The film morphology was characterized using a Gemini Ultra 55 (Zeiss, Germany) scanning electron microscope with a secondary electron (SE2) detector. An acceleration voltage of 2.0 kV was used. Micrographs were taken of the upside of the electrode layer (layer-atmosphere-interface). The electrode layer was transferred to the specimen holder together with the PET substrate.

For some layers, SEM analysis was not successful in evaluating the cracking degree (Chapter "Cracking area coverage via image analysis"), as too few or too many cracks were found. In these cases, images were taken with an optical microscope (Axio Imager M1m, Zeiss) to increase the evaluated area.

Cracking area coverage via image analysis

The degree of cracking was determined using image analysis by assessing the cracked area per image, referring to the total image area, by performing a grey-scale evaluation. Generally, SEM images recorded at a magnification of 100× were used to evaluate the cracking degree. However, in cases with very severe cracking and thus delamination of the PET substrate (which could cause damage in the SEM) and in cases with very few cracks, mosaic images (10 − 12 × 4) taken with the optical microscope at a magnification of 2.5× were used for the image analysis. At least two images per layer were evaluated.

Mercury intrusion porosimetry

Pore size distributions were measured using a PoreMaster GT (Quantachrome Instruments, USA) in two pressure regions (low-pressure region: 0.07–3.18 bar and high-pressure region: 1.4–3891.1 bar). An approximately 1 × 1 cm^2 sized layer on the PET substrate (~0.1–0.2 g) was analyzed. For the surface tension of mer-

Table 1

Compositions of carbon black/ionomer suspensions in 87/13 wt% DAA/water mixture (1, 3, 5, and 7 were prepared using both CB types; 2*, 4*, and 6* were prepared with only CB1).

	Ionomer to carbon weight ratio, I/C	Amount of carbon black (wt%)	Amount of ionomer (D79-25BS) (wt%)	Total solid content (wt%)
1	0	4.0	0.0	4.0
2*	0.1	4.0	0.4	4.4
3	0.2	4.0	0.8	4.8
4*	0.35	4.0	1.4	5.4
5	0.5	4.0	2.0	6.0
6*	0.75	4.0	3.0	7.0
7	1.0	4.0	4.0	8.0

cury and contact angle, values of 480 mN/m and 140° were used, respectively.

Results and discussion

Characterization of carbon blacks

Carbon black consists of primary particles with sizes in the range of 20–50 nm, which are covalently bonded together to aggregates with sizes in the range of 100–500 nm. These aggregates cluster loosely together to larger agglomerates in the size range of several μm (Soboleva et al., 2010). The "structure" of a carbon black aggregate is described by the degree of aggregation of the primary particles. "Highly branched" carbon blacks refer to very branched and chain-like aggregates consisting of many primary particles, whereas aggregates that consist of fewer primary particles are considered to exhibit a "less branched structure" (Lin & Chung, 2007).

The two used carbon black types (CB1 and CB2) differ mainly in their specific surface area and structure. The surface area was determined by nitrogen sorption measurements (Chapter "Carbon black powder characterization"). In Table 2, the specific surface area $S_{A,C}$ as well as the surface area of micropores $S_{MP,C}$, which were smaller than 2 nm, are given. Both the total specific surface area and accessible surface area were higher for CB2.

The oil adsorption numbers were determined according to D 2414-04 (ASTM International, 2004) and were provided by Greenerity GmbH (Table 2). Here, the amount of oil (dibutyl phthalate, DBP) which is absorbed by the carbon black was measured and expressed in mL/100 g of carbon black. Large oil adsorption numbers (OANs) represent a fractal aggregate structure and thus indicate a "higher branched" carbon black (Lin & Chung, 2007).

The form factors were determined by examining the carbon black structures using SEM (see Supplementary material 1). The CB2 particles were larger and had smaller form factors, indicating a more fractal structure of the carbon black aggregates.

In terms of the degree of amorphization, which was determined by Raman and XRD measurements (Supplementary material 2 and 3), both carbons showed very similar behavior (Table 3). Applying the classification of Ferrari and Robertson (2004) based on the I_D/I_G ratio and the G-peak position of the Raman spectra, both carbon blacks exhibited a carbon structure between that of nanocrystalline (NC) graphite and amorphous carbon black, with CB2 being slightly more graphitic than CB1. This trend also held for the d_{002} value,

which represents the distance between the graphite layers. For perfect graphite, the d_{002} value is 0.3354 nm (Richards, 1968).

Pycnometric density measurements revealed that CB2 exhibited a higher density, which also indicates its larger degree of graphitization compared with that of CB1, as perfect graphite has a density of $\sim$2.26 g/cm^3, whereas the densities of carbon black are usually between 1.7 and 1.9 g/cm^3 (Donnet, 1993; Kotlensky & Walker, 1960).

Effect on suspensions characteristics

Particle size distributions

The particle size distributions Q_3 of the carbon blacks in terms of cumulative volume distribution are shown in Fig. 1. When no ionomer was added ($I/C = 0$), the highly branched CB2 exhibited a slightly larger particle size because of its more branched structure (CB1: $x_{50,3} = 8.0$ μm; CB2: $x_{50,3} = 9.5$ μm). When ionomer was added, the particle size of both carbon blacks decreased, as the ionomer adsorbed onto the carbon black surface and stabilized the carbon black particles. Similar findings were also observed by Shukla et al. (2017). This effect was more pronounced for the CB2 suspension, where a significant increase of the fine fraction between 0.1 and 1 μm was observed, presumably because a larger surface area was provided for ionomer adsorption.

Viscosity and yield stress

The flow curves of the suspensions are presented in Fig. 2. All the suspensions exhibited shear thinning behavior. Because of its more branched structure, suspensions with CB2 exhibited significantly larger viscosities in the whole shear rate range up to $1000\,s^{-1}$. Similar behavior has also been observed by other groups (Barrie et al., 2004; Lin & Chung, 2007). Barrie et al. (2004) investigated the rheology of two carbon black suspensions, which were denoted as "fractal" and "spherical", and showed that the fractal carbon black led to higher viscosities than the spherical type. Lin and Chung (2007) reported that more branched carbon blacks, as indicated by their oil adsorption number, led to dispersions with higher viscosities. In our study, the addition of only a small amount of ionomer ($I/C = 0.1$) led to a slight decrease of the viscosity for the less branched CB1. When the ionomer content was further increased, an increase in the viscosity was observed (also Supplementary material 4 (viscosity is plotted as a function of I/C ratio for different shear rates)). We assume that owing to the adsorption of the ionomer on the carbon black, these particles are better stabilized in suspension, and therefore, the viscosity drops. Nevertheless, already

Table 2

Specific surface area and surface area of micropores determined by nitrogen adsorption, oil adsorption number, and form factor of used carbon black types.

	CB1	CB2
Specific surface area, $S_{A,C}$ (m^2/g)	223.6	773.3
Surface area of micropores, $S_{MP,C}$ (m^2/g)	83.5	486.0
Accessible surface area, $S_{A,C,access}$ (m^2/g)	140.1	287.3
Oil adsorption number (OAN) (mL/100 g)	200	320
Median form factor (50%) (image analysis)	0.93	0.72

Table 3

Structural properties of used carbon black types.

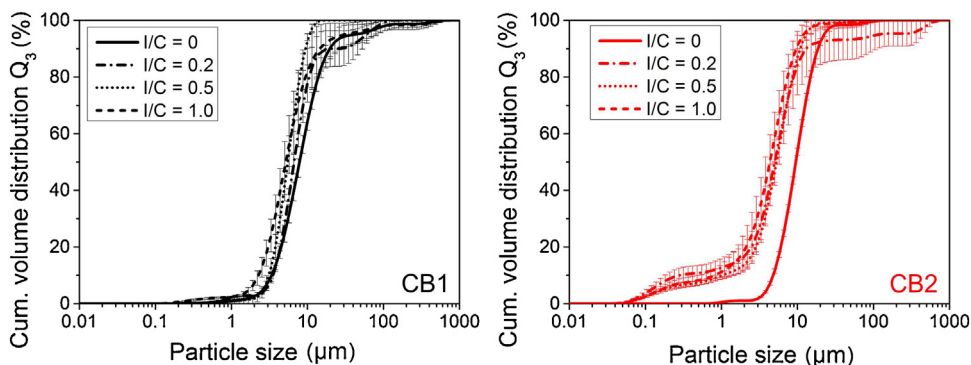|	CB1	CB2
I_D/I_G	1.16	1.23
G-position (cm^{-1})	1581.0	1583.0
d_{002} (nm)	0.3625	0.3598
Pycnometric density (g/cm^3)	1.99	2.20

Fig. 1. Particle size distributions of suspensions of CB1 (left) and CB2 (right) in a DAA/water mixture with varying ionomer content.

at an I/C of 0.2, a significant amount of ionomer is not adsorbing onto the carbon but stays in solution. This "excess" ionomer leads to additional interactions between ionomer molecules and, thus, higher viscosities. A similar trend was observed when the ionomer was added to the CB2 suspension; however, the differences were much more distinct. Increasing the I/C ratio from 0 to 0.2/0.5 resulted in a remarkable reduction of the viscosity, whereas further addition of the ionomer increased the viscosity again. The first significant drop in the viscosity at low I/C ratios has also been described by Mizukawa and Kawaguchi (2009) and is due to carbon black–ionomer interactions, which lead to break-up of the carbon black network into smaller and more stabilized particles. These well-stabilized particles better align in shear flow when shear stresses are applied and thus exhibit lower viscosities. Nevertheless, when the ionomer content is increased above a critical value (I/C ratio: 0.1 for CB1; 0.2/0.5 for CB2), the viscosity increases again, as ionomer–ionomer interactions of non-adsorbed ionomer molecules become more pronounced. As expected, the viscosity is a function of the suspension structure, which is determined by the overall solid content within the system as well as by the interactions between the carbon black and ionomer.

To evaluate the flow curves, we applied the Ostwald/de Waele power law (Eq. (2)) (Mezger, 2012) for shear rates between 1 and $10\,\mathrm{s}^{-1}$. This non-linear approach is often used to describe the rheological behaviors and relations of a non-Newtonian fluid in a simplified manner. Here, τ is the shear stress in Pa, $\dot{\gamma}$ is the shear rate in s^{-1}, κ is the so-called consistency factor in Pa s, and n (dimensionless) is the flow index. For $n = 1$, Newtonian flow behavior is observed; for $n < 1$, shear thinning is observed; and for $n > 1$, shear thickening is observed. The determination of the parameters n and κ using the Ostwald-de-Waele model is presented in Supplementary material 5–7.
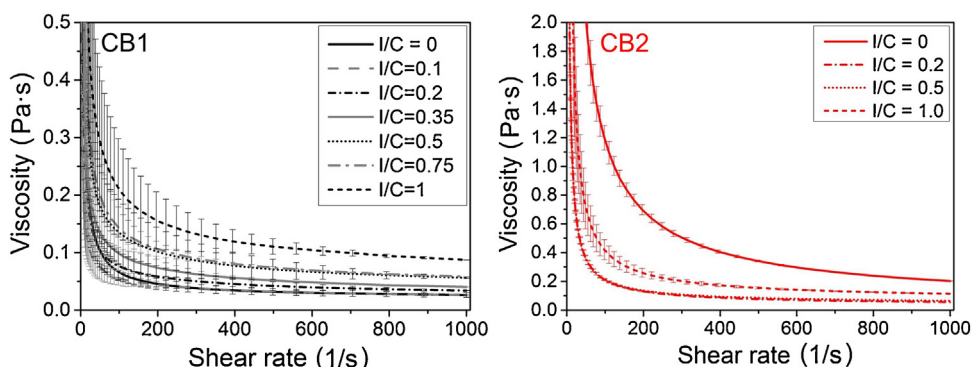
$$\tau = \kappa\dot{\gamma}^n. \qquad (2)$$

Fig. 3 (left) shows that at an I/C of 0, CB1 exhibits a smaller flow index n compared with that of CB2 and thus shows a larger degree of shear thinning, presumably because of a better alignment or even break-up of the carbon black particles in the flow field. For CB1, the flow index n remains almost constant (exception at $I/C = 0.35$) with increasing I/C ratio, indicating a constant degree of shear thinning over the whole I/C region. For the consistency factor κ, first a slight decrease when changing the I/C ratio from 0 to 0.1, followed by a steady increase with higher I/C ratios was observed. This finding is in agreement with the viscosity progression described earlier. For the CB2 suspensions, the flow index n continuously dropped with increasing I/C ratio, indicating that the CB2 suspensions exhibit a higher degree of shear thinning with increasing amount of ionomer. This is caused by both the break-up of carbon black particles and the alignment of the ionomer during shearing, although the break-up of the carbon–ionomer network leads to stronger shear thinning than the break-up of pure carbon agglomerates. The consistency factor κ is in line with the trend in viscosity: κ decreases first when changing the I/C ratio from 0 to 0.2 as the carbon black network is broken up and fragments are stabilized by the ionomer. When I/C is increased to values >0.5, an increase of κ is observed because of ionomer interactions.

Oscillation experiments were also performed (Supplementary material 8 and 9). Viscoelastic behavior was observed for all of the suspensions. As the storage modulus G' in Pa (elastic part) is always higher than the loss modulus G'' in Pa (viscous part), the suspension properties are dominated by the elastic behavior of the suspension. The values for the yield point extracted from the amplitude sweeps, which signify the shear stress at which irreversible structure deformation occurs, are shown in Fig. 3 (right). As observed earlier, an increase in the yield point with increasing I/C ratio was observed for the CB1 suspensions, as the non-adsorbed ionomer leads to additional intermolecular interactions and strengthens the gel-like character of the suspension. For the CB2 samples, a high yield point
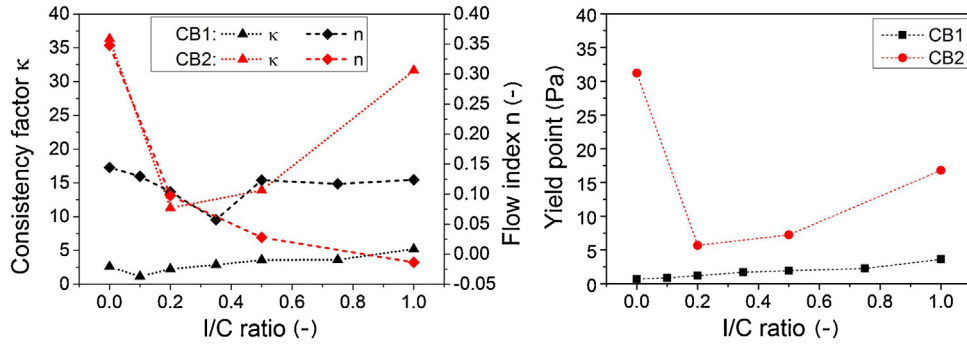

Fig. 2. Flow curves of suspensions of CB1 (left) and CB2 (right) in DAA/water mixture with varying ionomer content.

Fig. 3. Consistency factor κ, flow index n (left), and yield points (right) of CB1 and CB2 suspensions with varying ionomer content.

was measured in the absence of ionomer owing to the branched carbon black network, whereas a significant yield point drop was observed when a small amount of ionomer was added because of stabilization of the carbon black by the ionomer. For all I/C ratios >0, the yield stress was larger for the CB2 than for the CB1 suspensions, indicating that the CB2 network is clearly stronger than the CB1 network. This result is likely due to the branched CB2 particles highly interacting with each other, which results in the formation of stable network structures that are not as easy to break up compared with the more loosely bound CB1 particles.

Colloidal stability

As the amount of ionomer affects the internal structure of suspensions, as demonstrated by the rheological characterization, we conducted sedimentation tests to validate the change in colloidal stability with varying ionomer content.

Integral transmission curves were obtained by sedimentation analysis in an analytical centrifuge (an example is shown in Supplementary material 10 for I/C ratios of 0 and 1). Divergent end values for the integral transmission T_{end} were obtained for the different suspensions because of the colored supernatant of the samples. Therefore, a relative analysis, taking into account the transmission T_{end} of the supernatant, was needed to compare the different samples. We evaluated the transmission curves using the following growth function, where T is the integral transmission in % and t_{sed} is the sedimentation time in s; T_0 and T_{end} (in %) are the integral transmissions at the beginning and end of the centrifugation run, respectively; t_{50} (in s) is the time when 50% of T_{end} is reached; and f represents a dimensionless fitting parameter:

$$T = T_0 + \frac{(T_{\text{end}} - T_{0})}{1 + \left(\frac{t_{50}}{t_{\text{sed}}}\right)^f}. \tag{3}$$

The corresponding sedimentation time t_{50} at $T_{\text{end}}/2$ was determined using Eq. (3). As the sedimentation time t_{50} depends on the solvent viscosity η_S (in Pa s) as well as on the particle and solvent densities ρ_P and ρ_s (in kg/m^3), respectively, Hansen introduced a relative sedimentation time (RST) (in s^2/m^2), see Eq. (4), that accounts for these factors (Hansen, 2007):

$$RST = \frac{t_{50}\left(\rho_p - \rho_s\right)}{\eta_s}. \tag{4}$$

The calculated *RST* values are plotted versus the *I/C* ratio for both carbon blacks in Fig. 4.

Without the addition of ionomer ($I/C = 0$), the relative sedimentation time (RST) of the highly branched CB2 was longer than that of CB1, indicating a higher stability. Two effects might cause this behavior. Branching of the carbon black leads to the formation of a carbon network and thus sedimentation hindrance and swarm sedimentation effects (Stieß, 2001). In addition, the frictional ratio might play a role, as shown by Walter et al. (2015): anisotropic
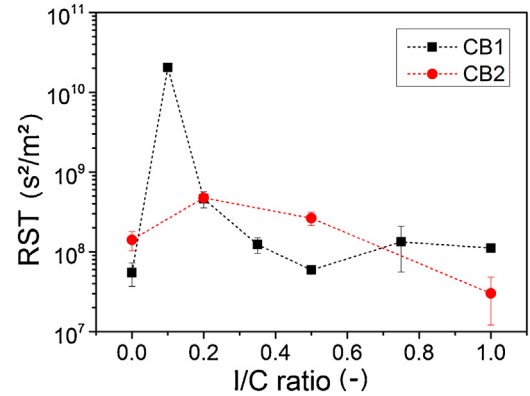

Fig. 4. Relative sedimentation times of CB1 and CB2 suspensions with varying ionomer content (carbon black concentration: 4 wt%).

particles, with a dimensionless frictional factor $f_t/f_0 > 1$, result in lower sedimentation coefficients s in sved (Eq. (5)), which in turn correlate to slower sedimentation velocities u in m/s (Eq. (6)):

$$\frac{V_p}{s}\left(\rho_p - \rho_s\right) = 3\pi\eta_s x_V \frac{f_t}{f_0}, \tag{5}$$

$$s = \frac{u}{\omega^2 r_{\text{rot}}}, \tag{6}$$

where V_p is the particle volume (in cm^3), ρ_p is the particle density (including a stabilizing or hydration shell around the particle) (in kg/m^3), ρ_s is the solvent density (in kg/m^3), η_s is the solvent viscosity (in Pa s), x_V is the volume equivalent particle diameter (in μm), ω is the angular velocity (in rad/s), and r_{rot} is the rotation radius (in mm).

For small I/C ratios ($I/C = 0.2$ or even $I/C = 0.1$ for CB1), a jump to larger *RST* values is observed for both carbon blacks compared with the ionomer-free suspensions, as the ionomer stabilizes smaller particles (see Fig. 1) and thus, according to Stokes, reduces the settling velocity. These findings are also in accordance with reports in the literature (Shukla et al., 2017). However, when more ionomer is added, the stability drops again, presumably because the high polymer content induces the formation of larger agglomerate structures, which results in faster sedimentation. The flocculation of carbon black particles at high ionomer concentration can be attributed to two destabilization effects, namely depletion flocculation or bridging flocculation (Fellows & Doherty, 2005). Depletion flocculation describes the process at high polymer concentrations when two particles approach each other such that no polymer fits in the volume between them. This process produces an osmotic force, removing the solvent between the particles and resulting in particle attachment. Bridging flocculation describes the fusion of particles by a high-molecular polymer, which adsorbs on two or more parti-
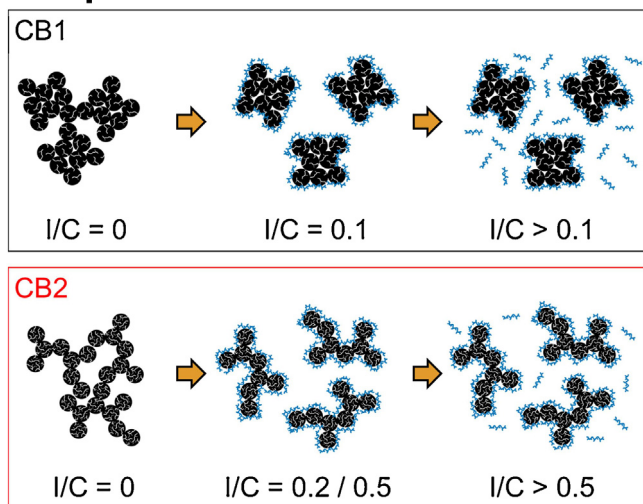
Suspension

Fig. 5. Model representation of suspension structure for CB1 and CB2 suspensions with varying ionomer content.

cles and physically holds them together (Fellows & Doherty, 2005). For CB1, a slight minimum in *RST* is observed at *I/C* = 0.5. We assume that increasing the ionomer content above this critical value leads to an increase of the *RST* again, as the high ionomer contents could result in swarm-sedimentation effects, where the settling velocity of the individual particles is hampered by the interaction of the displaced solvent volume elements (Stieß, 2001).

Model representation of suspension structure

With regard to the previously described findings, we derived a model representation of the internal suspension structure for both carbon black types and the different ionomer concentrations (Fig. 5).

CB1 exhibits a less branched structure, and the carbon black aggregates cluster loosely together. The ionomer adsorbs on the carbon black surface and thus stabilizes the carbon particles against re-agglomeration. Therefore, slightly smaller particle sizes are observed after comminution when the ionomer is added. At low ionomer concentrations, carbon aggregates are well stabilized in suspension, leading to a high colloidal stability and a low viscosity of the suspension. At larger ionomer contents, however, non-adsorbed free ionomer in the solvent phase leads to additional interactions between the free ionomer molecules, increasing the viscosity of the suspension and decreasing the colloidal stability. The particle size remains unchanged; however, because of the higher ionomer concentration, destabilization effects such as depletion flocculation or bridging flocculation might occur (Fellows & Doherty, 2005).

In contrast, the branched CB2 particles strongly interact with each other, resulting in high viscosities of the pure CB2 suspension. When ionomer is added, it adsorbs on the carbon black surface and stabilizes the aggregates against re-agglomeration, which results in a significant drop in the particle size and viscosity as well as improved colloidal stability as smaller particles settle more slowly. When the ionomer content is increased to *I/C* ratios higher than 0.5, the same mechanisms as those observed for CB1 occur; free ionomer again leads to an increase in viscosity and decrease in the stability of the suspension.

We thus suppose that less ionomer is needed to sufficiently stabilize the CB1 particles than the CB2 particles. This finding is also shown by yet unpublished results of our group, which present adsorption isotherms of the ionomer on different carbon blacks in

water. We used the amount of non-adsorbed ionomer in the solvent to draw a conclusion from the amount of adsorbed ionomer on the carbon black. The data were evaluated using the Langmuir adsorption model (Eq. (7)), where Γ_{eq} is the equilibrium coverage in g/g; Γ_{sat} is the saturation surface coverage in g/g; c_{eq} is the equilibrium concentration of non-adsorbed ionomer in the water phase in g/L; and K_{eq} is the association constant in L/g (Eq. (7)). We observed that the saturation surface coverage was significantly higher for CB2 than for CB1 ($\Gamma_{sat,CB1} = 0.045$ g/g, $\Gamma_{sat,CB2} = 0.063$ g/g), indicating that a larger amount of ionomer is adsorbing on CB2.

$$\Gamma_{eq} = \frac{\Gamma_{sat} c_{eq}}{\frac{1}{K_{eq}} + c_{eq}}. \tag{7}$$

As less ionomer adsorbs on the CB1 surface compared to CB2 at the same *I/C* ratio, more free ionomer is present in solution for the CB1 suspension and we observed an increase in viscosity already at smaller ionomer contents. When more ionomer adsorbs on the CB2 surface, more ionomer is necessary for sufficient stabilization and the effects observed for CB1 (increase of viscosity, decrease of *RST*) only occur at larger *I/C* values.

Effect of suspension properties on layer properties

The suspensions as characterized in Chapter "Effect on suspensions characteristics" were used to coat layers on a PET substrate via doctor blading.

Layer thicknesses, porosity, and cracking

After deposition of the carbon black/ionomer suspension onto a PET substrate with a doctor blade at different gap heights to vary the layer thickness, the suspension dries. While drying, the solvent evaporates; therefore, shrinkage occurs and the suspension converts from a liquid to a solid. During this solidification step, the suspension properties significantly change with regard to the structure and properties (Francis, Mccormick, Vaessen, & Payne, 2002). As observed in Fig. 6, the layer thickness depends not only on the adjusted gap height but also on the suspension composition. Thus, CB2 suspensions result in significantly larger layers and the addition of ionomer also reduces the layer thickness. The effects of the overall solid content, particle size, and viscosity on the layer thickness are discussed in Supplementary material 16–18.

When adding ionomer, even though the total amount of solids within the suspension increases, a decrease in layer thickness at constant gap heights occurs (Supplementary material 16), which is presumably due to the slight decrease in particle size and closer packing opportunity for those aggregates (Supplementary material 17). Nevertheless, this effect is only pronounced at very large gap heights. CB1 suspensions always result in thinner layers than CB2 suspensions, as the less-branched carbon particles can pack more closely, and therefore, denser layers are obtained. This finding is in agreement with those of Chiu, Garino, and Cima (1993), who also observed thicker layers with larger particles. We know that the viscosity of the suspension might also affect the initial wet film thickness directly after coating, as different viscosities might lead to different menisci at the edge of the doctor blade (Sullivan & Middleman, 1986). Nevertheless, no clear trend regarding the effect of the viscosity was observed in our study (Supplementary material 18). However, the CB2 samples generally exhibited a larger viscosity, which could result in smaller menisci at the doctor blade outlet and thus thicker wet film thicknesses.

As shown, the layer thickness mainly depends on the internal packing within the layer, which is primarily determined by the particle size of the carbon black particles. In Fig. 7 (left), the ratio between the relative layer thickness (actual layer thickness/gap height) and theoretical solid content (carbon black and ionomer)
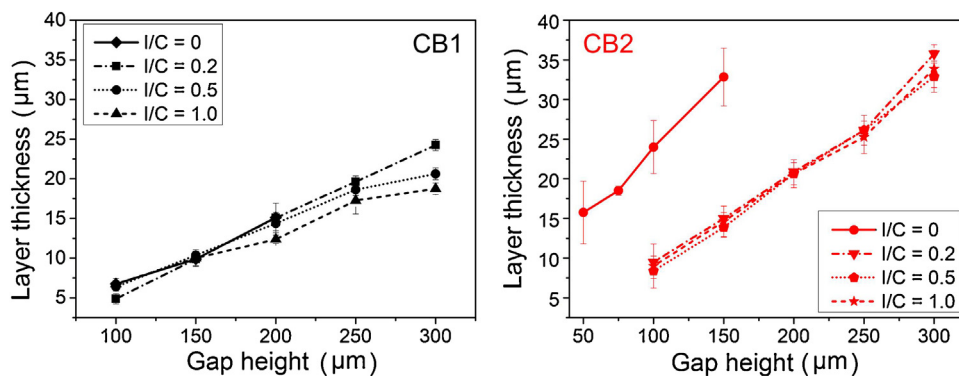
Fig. 6. Dependence of layer thickness on gap height for suspensions of CB1 (left) and CB2 (right) with varying ionomer content.
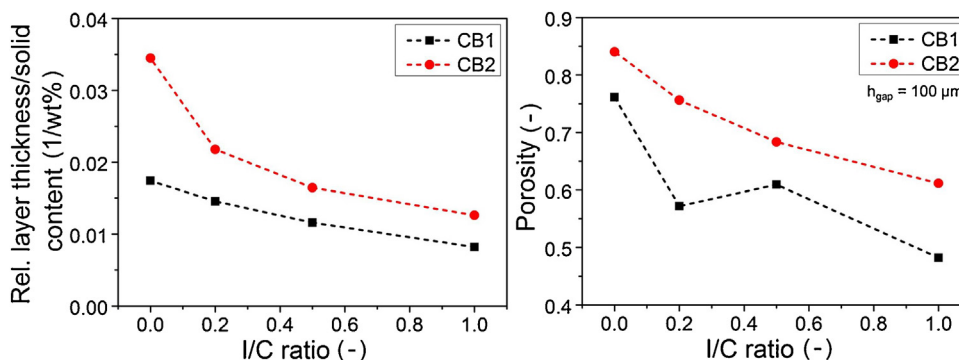

Fig. 7. Ratio between dry and wet layer thickness normalized to the overall solid content of CB1 and CB2 layers (left) and calculated porosity of CB1 and CB2 layers ($h_{gap} = 100 \mu m$) as a function of ionomer content (right).

of the suspensions is plotted versus the I/C ratio. The ratio steadily decreases with increasing I/C ratio for both carbon black types, hinting that with increasing ionomer content, the ionomer fills the pores of the carbon black layer and, thus, no additional accretion of the layer thickness is observed in the investigated I/C area. Furthermore, the larger layer thicknesses for the CB2 layer was evident for all the I/C ratios studied.

To evaluate the packing of the layers, the overall porosity ε (dimensionless) of the layers was calculated using Eq. (8), with ρ_{layer} and $\rho_{mixture}$ being the layer density and mixture density in kg/m³, respectively.

$$\varepsilon = 1 - \frac{\rho_{layer}}{\rho_{mixture}}. \tag{8}$$

The layer density was determined from the ratio between the loading of the layer X_{layer} (in g/cm³) and the layer thickness h_{layer} (in μm) (Eq. (9)). Both values were determined experimentally (Chapter "Film formation via doctor blading").

$$\rho_{layer} = \frac{X_{layer}}{h_{layer}}. \tag{9}$$

To estimate the mixture density, the initial weights $m_{ionomer}$ and $m_{carbonblack}$ (in g) for the ionomer and carbon black, respectively, used when preparing the suspension, were taken. Using an average value of the material densities for both materials ($\rho_{ionomer} = 2.0$ g/cm³; $\rho_{carbon\ black} = 1.9$ g/cm³), the ionomer volume $V_{ionomer}$ and carbon black volume $V_{carbon\ black}$ (in cm³) can be determined, and from these values, $\rho_{mixture}$ can be calculated (Eq. (10)).

$$\rho_{mixture} = \frac{m_{ionomer} + m_{carbon\ black}}{V_{ionomer} + V_{carbon\ black}}. \tag{10}$$

The results of the porosity calculations are depicted in Fig. 7 (right) for layers formed with a gap height of 100 μm. For the whole

I/C area, CB2 exhibits a larger porosity than CB1. Furthermore, for both carbon black types, the porosity decreases with increasing ionomer content, as the ionomer fills the pores between the carbon agglomerates. This effect has already been reported in the literature (Giorgi et al., 1998; Park et al., 2016; Uchida, 1996; Watanabe et al., 1985; Yu et al., 2015). Nevertheless, we must remark that the CB2 particles already exhibit a higher internal porosity because of their larger specific surface area and the measured porosity is only a global parameter, including both the internal particle porosity and porosity of the layer due to its packing.

Mercury intrusion measurements were also performed to determine the porosity of the layers (Fig. 8). We observed that the total amount of mercury and therefore the pore volume was larger for the CB2 layers than for the CB1 layers for all the I/C ratios. Additionally, a decrease in the amount of Hg was observed with increasing I/C ratio (Fig. 8, left). Both findings are in line with the calculated values (Fig. 7). The decrease in pore volume with increasing ionomer amount is consistent with the results of Uchida (1996). The trends underline our previous findings that the CB2 layers are more porous, and therefore, more mercury can enter the pores and the ionomer closes the pores within the layer, leading to a reduction in the maximal insertable Hg. The amount of mercury for the measurement of bare PET was very low, indicating the low porosity of our substrate, as expected. The pore size distributions of all the layers are provided in Supplementary material 19. Exemplarily, Fig. 8, right, shows the cumulative distributions of the CB1 layers with varying I/C ratio. We see that the pore size distributions of the layers are very multimodal, with pore sizes between ~7 nm and 1 μm, with the main fraction between ~20 and ~300 nm, corresponding mainly to macropores within the agglomerates (Soboleva et al., 2010). No significant differences in the pore size distributions of the layers were observed, indicating the uniform distribution of the ionomer, almost independent of the pore size.
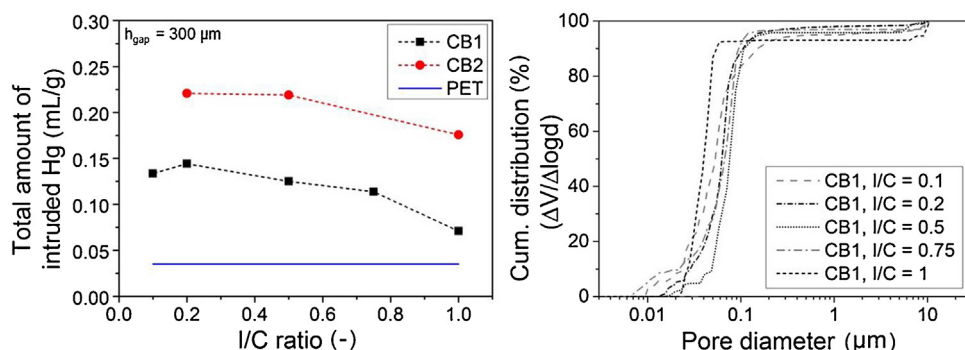
Fig. 8. Total amount of intruded mercury for CB1 and CB2 layers ($h_{gap} = 300\,\mu m$) and PET substrate (left) and cumulative pore size distributions of CB1 layers with varying ionomer content (right).
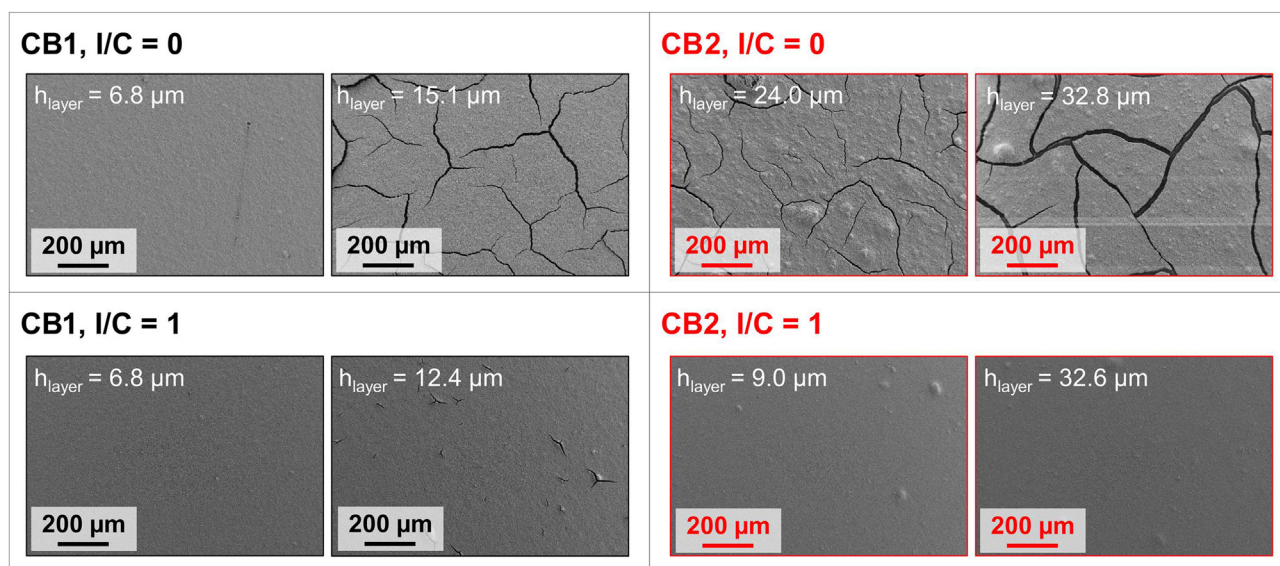

Fig. 9. SEM micrographs of CB1 layers (left) and CB2 layers (right) for I/C ratios of 0 and 1.

Fig. 9 presents eight exemplary SEM images of the upsides of the layers formed with the four different suspensions (CB1, CB2; $I/C = 0$, $I/C = 1$). Two films at different gap heights were always formed, resulting in different layer thicknesses of the dried layers h_{layer}. As observed in the micrographs, thicker layers contained more cracks. Moreover, it was observed that layers formed with only the rigid carbon black particles were very weak and fragile. The addition of ionomer improved the flexibility and strength of the layer.

In addition to the results that CB2 results in significantly thicker layers and the addition of ionomer leads to thinner films, it was also apparent that the addition of ionomer causes a reduction in cracking. For example, the 32.8 μm thick CB2 layer without ionomer exhibited a clear cracking pattern, whereas a layer of similar thickness (32.6 μm) with ionomer added ($I/C = 1$) showed no cracks.

To quantify the cracking degree, the cracking area was determined by image analysis of the SEM micrographs. For both CBs, the cracking degree increased with increasing layer thickness (Fig. 10). The increase of cracking with larger coating thicknesses was first described by Griffith (1921). Furthermore, the addition of ionomer led to a decrease in the cracking area coverage for both carbon black types, as previously illustrated in the SEM images. We define the layer thickness at which a cracking area coverage of 1% was observed as the critical coating thickness (CCT). The CCTs for each composition are listed in Table 4. A higher CCT was observed for CB2 than for CB1, indicating that cracks occur for CB2 at a larger layer thickness compared to CB1. We assume this finding results from

Table 4
Critical coating thicknesses for CB1 and CB2 layers with varying ionomer content, determined at cracking area coverage of 1%.

Ionomer to carbon weight ratio, I/C	CCT (μm)	
	CB1	CB2
0	10.2	19.3
0.2	11.4	23.8
0.35	14.0	
0.5	19.7	24.5
0.75	>19.3	
1.0	13.7	>32.5

the more branched structure of the CB2 aggregates, which cannot pack as closely as the CB1 aggregates. As a result, larger pores form between the particles, which affects the capillary pressure and thus the drying stress (Eqs. (11) and (13)). Similar findings have already been reported by other groups, which have demonstrated that larger particle sizes and/or flocculated particles increase the CCT of alumina and silica dispersions (Chiu et al., 1993; Guo & Lewis, 1999).

The development of drying stresses can lead to substrate curling, crack formation, or delamination from the substrate. If the critical drying stress is exceeded, cracks form (Francis et al., 2002). In conclusion, cracking in colloidal systems is driven by the interplay of capillary pressure and adhesion forces between the coating and substrate (Roberts & Francis, 2013; Singh & Tirumkudulu, 2007).
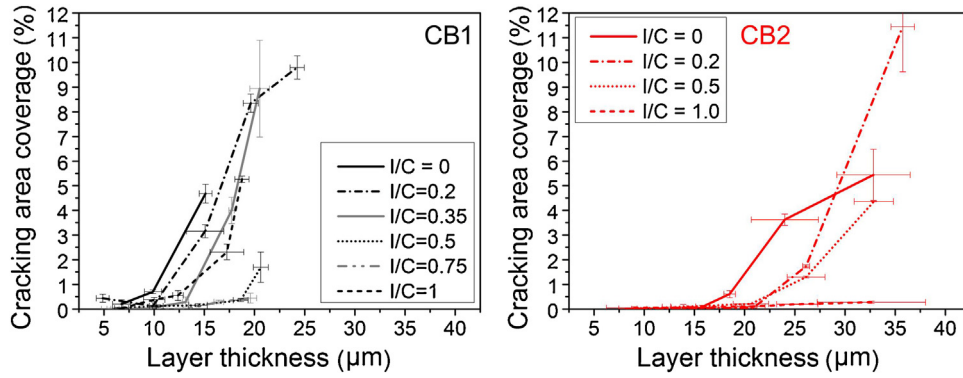
Fig. 10. Dependence of cracking degree on layer thickness for CB1 suspensions (left) and CB2 suspensions (right) with varying ionomer content.

Capillary forces arise when the liquid starts to recede into the particle network during drying, whereas the counteracting adhesion forces try to maintain the current shape and position of the coating (Francis et al., 2002). The negative capillary pressure puts the drying suspension in compression in the vertical direction and in tension along the horizontal axis (Russel, 2011). These strains lead to pore closing, particle deformation, and layer shrinkage (Francis et al., 2002). Generally, the capillary pressure p_{cap} (in Pa) in a capillary is defined by the Young–Laplace equation:

$$p_{cap} = \frac{2\gamma_L \cos\left(\theta_{SL}\right)}{r_p}, \tag{11}$$

where γ_L is the surface tension of the liquid in N/m, θ_{SL} is the contact angle between the solid and liquid in °, and r_p is the pore radius in μm. The capillary pressure arises when the particles are dewetted by the liquid during drying and works against the particle network strength. The interplay between the capillary pressure, particle network strength, and substrate affinity determine the cracking behavior of a system. As easily derived using Eq. (11), smaller particle sizes, which form narrower pore radii, and larger surface tensions lead to an increase of the capillary pressure. As in our experimental set-up, the solvent phase remains unchanged, the surface tension and contact angle are considered constant, and only the pore size changes as a result of the different structures of the two carbon black types. The CB2 layers are expected to exhibit larger pore radii because of their looser packing, which results in a reduced capillary pressure during drying and therefore fewer cracks. This finding is in agreement with the work of Singh et al. (2009), who investigated the cracking behavior of flocculated particle systems, where particles are clearly in contact with each other before the random close packing state. They showed that poorly stabilized particle systems result in lower packing volume fraction at the end of the drying step, which in turn yields increased CCTs because of the lower capillary pressure. Similar findings have been published by Chiu et al. (1993) and Guo and Lewis (1999), who showed that flocculated particle suspensions and suspensions with larger particles lead to larger pores, lower stress during drying, and increased CCTs.

As stated earlier, we found that with increasing amount of ionomer in the suspension, the layers exhibited less cracks even though the porosity of the layers decreased. Nevertheless, for the CB1 suspensions, a minimum in the cracking area coverage was observed for an I/C ratio of 0.5/0.75, whereas with an I/C of 1, the cracking increased again. Interestingly, the largest pore sizes of the layers were also found at I/C ratios of 0.5 and 0.75, whereas for an I/C of 1, smaller pores were observed (Fig. 8). According to Eq. (11), a larger pore radius leads to lower capillary stresses and therefore less cracking.

We used a mixture of soft (ionomer) and hard (carbon black) particles for layer formation. Soft particles tend to deform and therewith close the pores in a layer, whereas hard particles crack and thereby release drying stresses (Scherer, 1990; Singh & Tirumkudulu, 2007; Wu & Francis, 2017). Therefore, in colloidal slurries, the Young's modulus of the particle has a significant effect on the cracking behavior during drying. As soon as the strain energy release in a layer is higher than the energy needed for crack formation, cracks will form. Particles with lower Young's modulus are softer and therefore easily deformable, which reduces the cracking probability. The dependence of cracking on the Young's modulus was first described by Griffith (1921), who derived Eq. (12), also known as the Griffith criterion. Here, σ_c is the cracking stress (in Pa), E is Young's modulus (in Pa), γ_s is the surface energy of the material (in N/m), l_{flaw} is the length of a flaw/initiation crack (in m), and ν is Poisson's ratio (dimensionless).

$$\sigma_c = \sqrt{\frac{2E\gamma_s}{\pi l_{flaw}\nu}}. \tag{12}$$

As observed in Eq. (12), a lower Young's modulus directly leads to a reduction of the cracking stress. The Griffith criterion holds for linear elastic materials; however, for elastic plastic substances, the plasticity must be included when considering the fracture mechanics. Tirumkudulu and Russel (2005) used the Griffith criterion to balance the elastic energy release and increasing surface energy during cracking for latex dispersions to predict the critical cracking stress σ_{crit} (in Pa) and cracking spacing of a resulting layer, Eq. (13).

$$\frac{\sigma_{crit} r}{2\gamma_L} = 0.1877 \left(\frac{2r}{h_{layer}}\right)^{2/3} \left(\frac{GM\phi_{rcp} r}{2\gamma_L}\right)^{1/3}. \tag{13}$$

Here, r is the particle radius in μm, γ_L is the liquid surface tension in N/m, h_{layer} is the layer thickness in μm, G is the shear modulus of the particles in Pa, M is the dimensionless coordination number, and ϕ_{rcp} is the dimensionless volume fraction for random close packing of the particles (Tirumkudulu & Russel, 2005).

Singh and Tirumkudulu (2007) identified two distinct regimes for crack-free films. Depending on the rigidity of the particles (shear modulus G of the particles), they distinguished between a strain-limited case for soft particles (G small) and a stress-limited regime for hard particles (G high). The shear modulus G is connected to the Young's modulus E and Poisson's ratio as follows:

$$G = \frac{E}{2(1+\nu)}. \tag{14}$$

In the stress-limited regime for hard particles, the *CCT* (in μm) increases with particle rigidity (Eq. (15)). In this case, the *CCT* is also a function of the maximum attainable capillary pressure $p_{cap,max}$ (in Pa). In contrast, in the strain-limited regime for soft particles

(Eq. (16)), particles deform, and therefore, the *CCT* decreases with increasing particle rigidity (Singh & Tirumkudulu, 2007).

$$CCT = 0.64 \left(\frac{GM\phi_{\mathrm{rcp}}}{2\gamma_{\mathrm{L}}} \right)^{\frac{1}{2}} \left(\frac{2\gamma_{\mathrm{L}}}{-p_{\mathrm{cap,max}}} \right)^{\frac{3}{2}}, \tag{15}$$

$$CCT = \frac{37\gamma_{\mathrm{L}}}{GM\phi_{\mathrm{rcp}} \left(1 - \phi_{\mathrm{rcp}} \right)^3}. \tag{16}$$

For the stress-limited regime, the findings of Wu and Francis (2017) agree with the trend described by Singh and Tirumkudulu (2007). In their studies, calcium carbonate/latex mixtures showed a higher stress when a wide particle size distribution was used, as denser layers form in this case, yielding higher capillary pressures. Moreover, they found that the addition of latex yields higher drying stresses, and as latex with its lower glass transition temperature deforms more strongly during drying, higher drying stresses were observed (Wu & Francis, 2017).

We used Eq. (15) to calculate the maximum capillary pressure for pure carbon black layers ($I/C = 0$), (Supplementary material 20). As CB2 exhibits a higher porosity and therewith a lower volume fraction (neglecting the inner porosity of the pristine carbon black material) as well as a larger critical coating thickness *CCT*, lower maximum capillary pressures were calculated (CB1: $p_{\mathrm{cap,max}} = -551$ kPa; CB2: $p_{\mathrm{cap,max}} = -304$ kPa).

Generally, the ionomer acts as a binder within the system (Holdcroft, 2014). Because of its significantly lower Young's modulus of ~0.6 GPa (for Aquivion 850 at 25 °C) (Zhao & Benziger, 2013) and shear modulus of ~0.2 GPa (Poisson's ratio for Nafion: $\nu = 0.5$ (Jalani & Datta, 2005)) compared with those of the rigid carbon black particles (Young's modulus of ~4–28 GPa and shear modulus of ~1.7–11.5 GPa (AZoNetwork UK Ltd., 2001)), the drying stresses occurring during evaporation of the solvent can be dissipated by deformation of the ionomer instead of cracking of the layer (Griffith criterion, Eq. (12)). In Fig. 10, a reversal of that trend is observed for the CB1 suspensions for I/C ratios between 0.5 and 1.0. We assume that with very high ionomer contents, the pores between and within the aggregates become filled with ionomer; therefore, the pore radius decreases again, leading to an increase in the capillary pressure according to Young–Laplace and thus more cracks within the layer. For the CB2 suspensions, however, this effect is not observable in the investigated I/C region, as the pores are clearly larger.

Drying stresses

A common method used to measure drying stresses is the cantilever deflection method, where slurry is coated on an elastic substrate. The drying stresses lead to deformation of the substrate during the drying process, and the curvature of the substrate is recorded. Advantageously, the mechanical properties of the coating do not need to be known to determine its stress (Francis et al., 2002). As cantilever bending does not only depend on the drying stress but also on the mass on top of the cantilever, Fu et al. (2015) modified the original Corcoran equation (Corcoran, 1969) by considering the impact of the mass loss due to solvent evaporation on the cantilever curvature. Eq. (17) is used to determine the drying stress $\sigma(t)$ in Pa during a drying process, with the cantilever bending $d(t)$ in mm, the coating mass loss $\Delta m(t)$ in g, the gravitational acceleration g (9.81 m/s²), the width of the substrate b in mm, the effective length of the substrate L in mm, the Young's modulus of the substrate E_{s} in Pa, the dimensionless Poisson's ratio of the substrate ν_{s}, the cantilever thickness h_{s} in μm, and the coating thickness $h_{\mathrm{c}}(t)$ in μm.

$$\sigma(t) = \frac{\left(d(t) - \left(3\Delta m(t) g L^3 / \left(2E_{\mathrm{s}} b h_{\mathrm{s}}^3 \right) \right) \right) E_{\mathrm{s}} h_{\mathrm{s}}^3}{3h_{\mathrm{c}}(t) L^2 (h_{\mathrm{s}} + h_{\mathrm{c}}(t))(1 - \nu_{\mathrm{s}})}. \tag{17}$$

As the drying stresses impact the crack formation during layer formation, the mass loss, layer shrinkage, and drying stress as a function of drying time are depicted in Fig. 11 for four suspensions with CB1 and CB2 and I/C ratios of 0 and 1 using the cantilever setup described by Fu et al. (2015). During drying, the solvent evaporates, and therefore, mass loss and layer shrinkage are detected. As soon as the suspension reaches its closest packing and the liquid recedes into the interior of the film, drying stresses are generated, which are also measured.

We should state that the cantilever deflection measurements without the addition of the ionomer ($I/C = 0$) were challenging because of the severe cracking of the layers, which led to fluctuating results. Moreover, as the coating dries laterally, meaning that drying starts at the edges of the film and propagates to the interior of the film, non-uniform stress development is expected (Price, Wu, McCormick, Francis, & Scherer, 2015), which was not considered in our evaluation, as only the global stress evolution was measured.

In all cases, a steady increase in the drying stress with drying time was observed. Whereas the layers with an I/C of 0 both exhibited severe cracking, no cracks were observed when using an I/C ratio of 1. Higher drying stresses were generated for the CB1 samples for the experiments both with and without the ionomer. This result agrees with our expectations: according to Young–Laplace (Eq. (11)) and our calculations (Supplementary material 20), smaller pores (CB1) result in larger capillary pressures, and therefore, higher drying stresses are observed. Guo and Lewis (1999) reported similar results; they studied the aggregation effect of silica suspensions on the drying behavior and demonstrated that a flocculated particle suspension led to larger pores and thus lower stress during drying.

When comparing the different I/C ratios, lower drying stresses were measured when no ionomer was added, as the stresses were released by cracking and not by bending of the cantilever. This finding is in line with the results of Fu et al. (2015), who could show that for Al₂O₃ suspensions, the addition of binder (PVB) led to a reduction of the porosity and thus an increase in the drying stress. Moreover, they found that using smaller particles resulted in higher viscosities of the slurry and increased drying stresses for SiO₂ suspensions. In terms of layer thickness, larger end layer thicknesses were observed for the CB2 layers (25%–28%) than for the CB1 layers (14%–16%), independent of the ionomer content. This finding was previously also observed in our doctor blading experiments (Chapter "Layer thicknesses, porosity, and cracking"). Nevertheless, the actual layer thicknesses between the layers formed via doctor blading and the cantilever method clearly differed (Supplementary material 22). Moreover, the CB2 layers required significantly longer drying times until the final layer thickness was achieved for $I/C = 0$ (~100 min) compared with the CB1 layers (~60 min). In contrast, with an I/C of 1, the end layer thickness was achieved after ~75 min for both carbon blacks.

With regard to mass loss, the CB2 layer required longer drying times (>175 min) for $I/C = 0$, whereas for CB1, the drying only requires ~100 min. Interestingly, the opposite trend was observed when the ionomer was added: the CB1 layer required a longer drying times (~150 min), whereas the CB2 layer was already fully dried after approximately 100 min. The final end mass was higher for both $I/C = 1$ layers (~10%), as the solid amount was twice as high ($c_{\mathrm{total}} = 8$ wt%) as for the pure carbon black suspensions ($c_{\mathrm{CB}} = 4$ wt%), where the relative end mass was ~5%. We assume that at an I/C of 0, drying of the CB2 requires a long time because the layer is very thick, which decelerates solvent evaporation, and the end layer thickness is only achieved after long drying times. As we expect the pores to be smaller for the CB1 layer, for $I/C = 1$, mass transport through the pores is slower for CB1 than for CB2 according to the Carman–Kozeny relation (Scherer, 1990), and therefore, longer drying times are required for CB1.
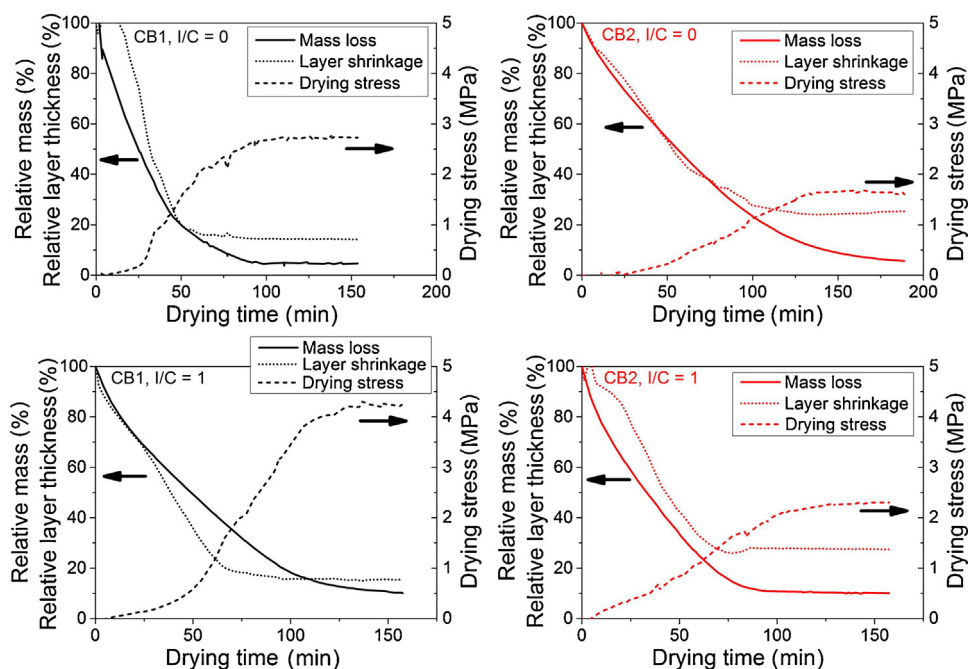
Fig. 11. Mass loss, layer shrinkage, and drying stress as a function of drying time determined using the cantilever deflection method for CB1 suspension (left) and CB2 suspension (right) for I/C = 0 (up) and I/C = 1 (down) (the standard deviations are not plotted for better visibility but can be found in Supplementary material 21).
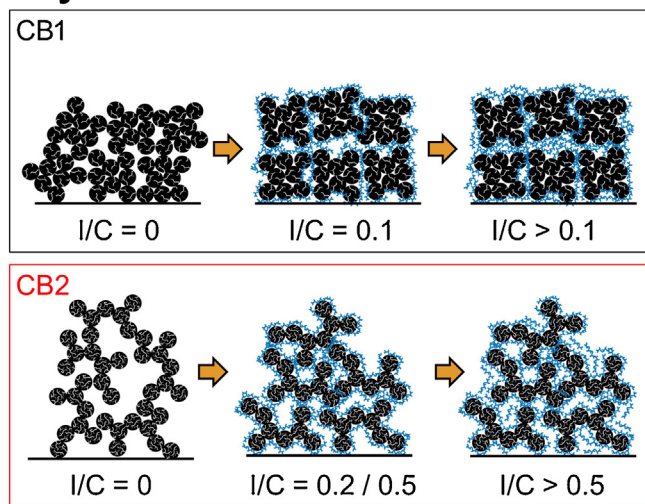
Layer

Fig. 12. Model representation of CB1 and CB2 layers with varying ionomer content.

Model representation of layer structure

As for the suspension structure, we also derived a model representation of the internal layer structure with regard to the previously described findings (Fig. 12).

For pure carbon black layers, when no ionomer is added, the classical drying theory applies, which indicates that a higher-branched carbon black leads to a more porous layer with larger pore sizes, which results in smaller capillary pressures and thus reduces the cracking. Moreover, as the branched carbon blacks cannot pack as closely as the less branched carbon black, thicker layers are obtained. When increasing the ionomer amount within the suspension, the slightly smaller particles can pack into denser layers, and the film thickness and porosity are thus reduced. Nevertheless, even though the porosity decreases, less cracking is observed. Because of the low Young's modulus of the ionomer, drying stresses deform the ionomer instead of inducing cracking of the layer. How-

ever, for the less branched carbon black CB1 with lower porosity, the addition of too much ionomer does not lead to further crack reduction but to an increase of cracking, as the pore size effect then dominates over ionomer deformation.

Conclusions

In this study, we systematically characterized the suspension and layer properties for the process chain of the production of pseudo-catalyst layers for PEMFCs. We observed that the carbon black structure and the ionomer amount not only affect the suspension viscosity and stability but also have a remarkable effect on the layer morphology.

Two types of carbon black (CB1 and CB2) with similar graphitization degrees that significantly differed in their spatial structures were used. Use of the higher branched carbon black (CB2), with larger specific surface area and higher oil adsorption number, resulted in suspensions with higher viscosity and colloidal stability. The layers of CB2 were thicker and more porous than those using the less branched CB1. The more branched structure of CB2 ensures a very porous layer with larger pores than those for the CB1 layers. These larger pores also affected the cracking behavior of the layers. For layers with CB2, higher CCTs were observed than for CB1, as larger pores lead to lower capillary pressures and thus lower cracking stresses.

When adding ionomer to the suspensions, the particle size of the less branched CB1 did not significantly change. In terms of viscosity, a slight decrease was first observed at small I/C (≈ 0.1); then, the viscosity increased again upon further increasing the ionomer amount. Presumably, only a small amount of ionomer adsorbs on the carbon black surface, whereas the main part stays in solution, increasing the suspension viscosity. Increasing I/C for the highly branched CB2 led to a much more pronounced decrease of the viscosity, as the particles were better stabilized by the ionomer, leading to smaller agglomerates. The addition of ionomer also reduced the layer thickness, especially for highly branched carbon blacks, as smaller particles can form denser layers. A reduced degree of cracking and larger CCTs were observed for both carbon

black types when adding the ionomer. The ionomer acts as a binder, releasing the drying stresses by deformation, and therefore, fewer cracks are formed. We found that the optimum amount of ionomer depends on the carbon black structure. For the less branched carbon black (CB1), more cracks appeared when exceeding an I/C ratio of 0.75, presumably because of pore closing resulting from the ionomer causing larger capillary pressures.

In terms of crack avoidance, highly branched carbon blacks should be favored in suspension formulation, as higher porosities and less cracking are observed. Moreover, because of their higher viscosity in suspension, layer formation is facilitated, as spreading on the substrate is hindered.

Declaration of interests

None.

Acknowledgements

Appendix A. Supplementary data

Supplementary data associated with this article can be found, in the online version, at https://doi.org/10.1016/j.partic.2018.08.001.

References

Ahn, C. Y., Jang, S., Cho, Y. H., Choi, J., Kim, S., & Kim, S. M. (2018). Guided cracking of electrodes by stretching prism-patterned membrane electrode assemblies for high-performance fuel cells. *Scientific Reports*, 8(1), 1257.

Andersen, S. M., Borghei, M., Dhiman, R., Ruiz, V., Kauppinen, E., & Skou, E. (2014). Adsorption behavior of perfluorinated sulfonic acid ionomer on highly graphitized carbon nanofibers and their thermal stabilities. *The Journal of Physical Chemistry C*, 118(20), 10814–10823.

ASTM International. (2004). *Standard test method for carbon black—Oil absorption number (OAN)*. ASTM D 2414-04, West Conshohocken, USA

AZoNetwork UK Ltd. (2001). *Carbon—Graphite materials.*. Retrieved from. https://www.azom.com/properties.aspx?ArticleID=516

Barrie, C. L., Griffiths, P. C., Abbott, R. J., Grillo, I., Kudryashov, E., & Smyth, C. (2004). Rheology of aqueous carbon black dispersions. *Journal of Colloid and Interface Science*, 272(1), 210–217.

Bender, G., Zawodzinski, T. A., & Saab, A. P. (2003). Fabrication of high precision PEFC membrane electrode assemblies. *Journal of Power Sources*, 124(1), 114–117.

Brunauer, S., Emmett, P. H., & Teller, E. (1938). Adsorption of gases in multimolecular layers. *Journal of the American Chemical Society*, 60(2), 309–319.

Chiu, R. C., Garino, T. J., & Cima, M. J. (1993). Drying of granular ceramic films: I, Effect of processing variables on cracking behavior. *Journal of the American Ceramic Society*, 76(9), 2257–2264.

Corcoran, E. M. (1969). Determining stresses in organic coatings using plate beam deflection. *Journal of Paint Technology*, 41, 635–640.

Detloff, T., Sobisch, T., & Lerche, D. (2007). Particle size distribution by space or time dependent extinction profiles obtained by analytical centrifugation (concentrated systems). *Powder Technology*, 174(1–2), 50–55.

Donnet, J. B. (Ed.). (1993). *Carbon black: Science and technology*. New York: Dekker.

Eguchi, M., Baba, K., Onuma, T., Yoshida, K., Iwasawa, K., Kobayashi, Y., et al. (2012). Influence of ionomer/carbon ratio on the performance of a polymer electrolyte fuel cell. *Polymers*, 4(4), 1645–1656.

Fellows, C. M., & Doherty, W. O. S. (2005). Insights into bridging flocculation. *Macromolecular Symposia*, 231(1), 1–10.

Ferrari, A. C., & Robertson, J. (2004). Raman spectroscopy of amorphous, nanostructured, diamond-like carbon, and nanodiamond. *Philosophical Transactions of The Royal Society A: Mathematical Physical and Engineering Sciences*, 362(1824), 2477–2512.

Francis, L. F., Mccormick, A. V., Vaessen, D. M., & Payne, J. A. (2002). Development and measurement of stress in polymer coatings. *Journal of Materials Science*, 37(22), 4717–4731.

Fu, Z., Eckstein, U., Dellert, A., & Roosen, A. (2015). In situ study of mass loss, shrinkage and stress development during drying of cast colloidal films. *Journal of the European Ceramic Society*, 35(10), 2883–2893.

Gallo Stampino, P., Cristiani, C., Dotelli, G., Omati, L., Zampori, L., Pelosato, R., et al. (2009). Effect of different substrates, inks composition and rheology on coating deposition of microporous layer (MPL) for PEM-FCs. *Catalysis Today*, 147, S30–S35.

Giorgi, L., Antolini, E., Pozio, A., & Passalacqua, E. (1998). Influence of the PTFE content in the diffusion layer of low-Pt loading electrodes for polymer electrolyte fuel cells. *Electrochimica Acta*, 43(24), 3675–3680.

Gode, P., Jaouen, F., Lindbergh, G., Lundblad, A., & Sundholm, G. (2003). Influence of the composition on the structure and electrochemical characteristics of the PEFC cathode. *Electrochimica Acta*, 48(28), 4175–4187.

Griffith, A. A. (1921). The phenomena of rupture and flow in solids. *Philosophical Transactions of the Royal Society of London. Series A: Containing Papers of a Mathematical or Physical Character*, 221, 163–198.

Guo, J. J., & Lewis, J. A. (1999). Aggregation effects on the compressive flow properties and drying behavior of colloidal silica suspensions. *Journal of the American Ceramic Society*, 82(9), 2345–2358.

Hansen, C. M. (2007). *Hansen solubility parameters: A user's handbook* (2nd ed.). Boca Raton: Taylor & Francis. Retrieved from. http://site.ebrary.com/lib/alltitles/docDetail.action?docID=10176660

Holdcroft, S. (2014). Fuel cell catalyst layers: A polymer science perspective. *Chemistry of Materials*, 26(1), 381–393.

Huang, D. C., Yu, P. J., Liu, F. J., Huang, S. L., Hsueh, K. L., Chen, Y. C., et al. (2011). Effect of dispersion solvent in catalyst ink on proton exchange membrane fuel cell performance. *International Journal of Electrochemical Science*, 6(7), 2551–2565.

Jalani, N. H., & Datta, R. (2005). The effect of equivalent weight, temperature, cationic forms, sorbates, and nanoinorganic additives on the sorption behavior of Nafion®. *Journal of Membrane Science*, 264(1–2), 167–175.

Jeon, S., Lee, J., Rios, G. M., Kim, H. J., Lee, S. Y., Cho, E., et al. (2010). Effect of ionomer content and relative humidity on polymer electrolyte membrane fuel cell (PEMFC) performance of membrane-electrode assemblies (MEAs) prepared by decal transfer method. *International Journal of Hydrogen Energy*, 35(18), 9678–9686.

Jung, C. Y., Kim, W. J., & Yi, S. C. (2012). Optimization of catalyst ink composition for the preparation of a membrane electrode assembly in a proton exchange membrane fuel cell using the decal transfer. *International Journal of Hydrogen Energy*, 37(23), 18446–18454.

Komoda, Y., Okabayashi, K., Nishimura, H., Hiromitsu, M., Oboshi, T., & Usui, H. (2009). Dependence of polymer electrolyte fuel cell performance on preparation conditions of slurry for catalyst layers. *Journal of Power Sources*, 193(2), 488–494.

Kotlensky, W. V., & Walker, P. L. (1960). Crystallographic and physical changes of some carbons upon oxidation and heat treatment. In *4th conference in carbon proceedings* (2. ed., rev. and expanded, pp. 423–442).

Kreuer, K. D., Schuster, M., Obliers, B., Diat, O., Traub, U., Fuchs, A., et al. (2008). Short-side-chain proton conducting perfluorosulfonic acid ionomers: Why they perform better in PEM fuel cells. *Journal of Power Sources*, 178(2), 499–509.

Lai, C. M., Lin, J. C., Ting, F. P., Chyou, S. D., & Hsueh, K. L. (2008). Contribution of Nafion loading to the activity of catalysts and the performance of PEMFC. *International Journal of Hydrogen Energy*, 33(15), 4132–4137.

Lee, D., & Hwang, S. (2008). Effect of loading and distributions of Nafion ionomer in the catalyst layer for PEMFCs. *International Journal of Hydrogen Energy*, 33(11), 2790–2794.

Lin, C., & Chung, D. D. L. (2007). Effect of carbon black structure on the effectiveness of carbon black thermal interface pastes. *Carbon*, 45(15), 2922–2931.

Ma, S., Chen, Q., Jogensen, F., Stein, P., & Skou, E. (2007). 19F NMR studies of Nafion™ ionomer adsorption on PEMFC catalysts and supporting carbons. *Solid State Ionics*, 178(29–30), 1568–1575.

Marrony, M., Beretta, D., Ginocchio, S., Nedellec, Y., Subianto, S., & Jones, D. J. (2013). Lifetime prediction approach applied to the Aquivion™ short side chain perfluorosulfonic acid ionomer membrane for intermediate temperature proton exchange membrane fuel cell application. *Fuel Cells*, 13(6), 1146–1154.

Mauritz, K. A., & Moore, R. B. (2004). State of understanding of Nafion. *Chemical Reviews*, 104(10), 4535–4586.

Mezger, T. (2012). *Das Rheologie-Handbuch: Für Anwender von Rotations- und Oszillations-Rheometern (4. Aufl.) Farbe und Lack Edition*. Hannover: Vincentz Network.

Mizukawa, H., & Kawaguchi, M. (2009). Effects of perfluorosulfonic acid adsorption on the stability of carbon black suspensions. *Langmuir*, 25(20), 11984–11987.

Ngo, T. T., Yu, T. L., & Lin, H. L. (2013). Influence of the composition of isopropyl alcohol/water mixture solvents in catalyst ink solutions on proton exchange membrane fuel cell performance. *Journal of Power Sources*, 225, 293–303.

Park, Y. C., Kakinuma, K., Uchida, H., Watanabe, M., & Uchida, M. (2015). Effects of short-side-chain perfluorosulfonic acid ionomers as binders on the performance of low Pt loading fuel cell cathodes. *Journal of Power Sources, 275*, 384–391.

Park, Y. C., Tokiwa, H., Kakinuma, K., Watanabe, M., & Uchida, M. (2016). Effects of carbon supports on Pt distribution, ionomer coverage and cathode performance for polymer electrolyte fuel cells. *Journal of Power Sources, 315*, 179–191.

Passalacqua, E., Lufrano, F., Squadrito, G., Patti, A., & Giorgi, L. (2001). Nafion content in the catalyst layer of polymer electrolyte fuel cells: Effects on structure and performance. *Electrochimica Acta, 46*(6), 799–805.

Perera, D. Y., & van den Eynde, D. (1983). Solvent influence on the development of internal stress in a thermoplastic coating. *Journal of Coatings Technology, 55*(699), 37–43.

Peron, J., Edwards, D., Haldane, M., Luo, X., Zhang, Y., Holdcroft, S., et al. (2011). Fuel cell catalyst layers containing short-side-chain perfluorosulfonic acid ionomers. *Journal of Power Sources, 196*(1), 179–181.

Price, K. K., Wu, Y., McCormick, A. V., Francis, L. F., & Scherer, G. (2015). Stress development in hard particle coatings in the absence of lateral drying. *Journal of the American Ceramic Society, 98*(7), 2214–2222.

Richards, B. P. (1968). Relationships between interlayer spacing, stacking order and crystallinity in carbon materials. *Journal of Applied Crystallography, 1*(1), 35–48.

Roberts, C. C., & Francis, L. F. (2013). Drying and cracking of soft latex coatings. *Journal of Coatings Technology and Research, 10*(4), 441–451.

Russel, W. B. (2011). Mechanics of drying colloidal dispersions: Fluid/solid transitions, skinning, crystallization, cracking, and peeling. *AIChE Journal, 57*(6), 1378–1385.

Sasikumar, G., Ihm, J. W., & Ryu, H. (2004). Dependence of optimum Nafion content in catalyst layer on platinum loading. *Journal of Power Sources, 132*(1–2), 11–17.

Scherer, G. W. (1990). Theory of drying. *Journal of the American Ceramic Society, 73*(1), 3–14.

Shukla, S., Bhattacharjee, S., Weber, A. Z., & Secanell, M. (2017). Experimental and theoretical analysis of ink dispersion stability for polymer electrolyte fuel cell applications. *Journal of The Electrochemical Society, 164*(6), F600–F609.

Singh, K. B., Bhosale, L. R., & Tirumkudulu, M. S. (2009). Cracking in drying colloidal films of flocculated dispersions. *Langmuir, 25*(8), 4284–4287.

Singh, K. B., & Tirumkudulu, M. S. (2007). Cracking in drying colloidal films. *Physical Review Letters, 98*(21), 218302.

Soboleva, T., Zhao, X., Malek, K., Xie, Z., Navessin, T., & Holdcroft, S. (2010). On the micro-, meso-, and macroporous structures of polymer electrolyte membrane fuel cell catalyst layers. *ACS Applied Materials & Interfaces, 2*(2), 375–384.

Stieß, M. (2001). *Mechanische Verfahrenstechnik* (korr. Nachdr). Springer: Berlin.

Sullivan, T. M., & Middleman, S. (1986). Film thickness in blade coating of viscous and viscoelastic liquids. *Journal of Non-Newtonian Fluid Mechanics, 21*(1), 13–38.

Tirumkudulu, M. S., & Russel, W. B. (2005). Cracking in drying latex films. *Langmuir, 21*(11), 4938–4948.

Uchida, M. (1995). New preparation method for polymer-electrolyte fuel cells. *Journal of the Electrochemical Society, 142*(2), 463–468.

Uchida, M. (1996). Effects of microstructure of carbon support in the catalyst layer on the performance of polymer-electrolyte fuel cells. *Journal of the Electrochemical Society, 143*(7), 2245–2252.

Uchida, M. (1998). Improved preparation process of very-low-platinum-loading electrodes for polymer electrolyte fuel cells. *Journal of the Electrochemical Society, 145*(11), 3708–3713.

Walter, J., Nacken, T. J., Damm, C., Thajudeen, T., Eigler, S., & Peukert, W. (2015). Determination of the lateral dimension of graphene oxide nanosheets using analytical ultracentrifugation. *Small, 11*(7), 814–825.

Watanabe, M., Tomikawa, M., & Motoo, S. (1985). Experimental analysis of the reaction layer structure in a gas diffusion electrode. *Journal of Electroanalytical Chemistry and Interfacial Electrochemistry, 195*(1), 81–93.

Wawra, S. E., Thoma, M., Walter, J., Lübbert, C., Thajudeen, T., Damm, C., et al. (2018). Ionomer and protein size analysis by analytical ultracentrifugation and electrospray scanning mobility particle sizer. *European Biophysics Journal, 47*(7), 777–787.

Wilson, M. S., & Gottesfeld, S. (1992). Thin-film catalyst layers for polymer electrolyte fuel cell electrodes. *Journal of Applied Electrochemistry, 22*(1), 1–7.

Wu, Y., & Francis, L. F. (2017). Effect of particle size distribution on stress development and microstructure of particulate coatings. *Journal of Coatings Technology and Research, 14*(2), 455–465.

Yang, T. H., Yoon, Y. G., Park, G. G., Lee, W. Y., & Kim, C. S. (2004). Fabrication of a thin catalyst layer using organic solvents. *Journal of Power Sources, 127*(1–2), 230–233.

Yu, H., Roller, J. M., Mustain, W. E., & Maric, R. (2015). Influence of the ionomer/carbon ratio for low-Pt loading catalyst layer prepared by reactive spray deposition technology. *Journal of Power Sources, 283*, 84–94.

Zhao, N., Edwards, D., Lei, C., Wang, K., Li, J., Zhang, Y., et al. (2013). The importance of water transport on short-side chain perfluorosulfonic acid membrane fuel cells operating under low relative humidity. *Journal of Power Sources, 242*, 877–883.

Zhao, Q., & Benziger, J. (2013). Mechanical properties of perfluoro sulfonated acids: The role of temperature and solute activity. *Journal of Polymer Science Part B: Polymer Physics, 51*(11), 915–925.